NANO LETTERS

LETTER

pubs.acs.org/NanoLett

Direct Quantification of the Mechanical Anisotropy and Fracture of an Individual Exoskeleton Layer via Uniaxial Compression of Micropillars

Lin Han,[†] Lifeng Wang,[‡] Juha Song,[†] Mary C. Boyce,[‡] and Christine Ortiz[†,*]

[†]Department of Materials Science and Engineering and [‡]Department of Mechanical Engineering Massachusetts Institute of Technology, 77 Massachusetts Avenue, Cambridge, Massachusetts 02139, United States

ABSTRACT: A common feature of the outer layer of protective biological exoskeletons is structural anisotropy. Here, we directly quantify the mechanical anisotropy and fracture of an individual material layer of a hydroxyapatite-based nanocomposite exoskeleton, the outmost ganoine of *Polypterus senegalus* scale. Uniaxial compression was conducted on cylindrical micropillars of ganoine fabricated via focused ion beam at different orientations relative to the hydroxyapatite rod long axis ($\theta = 0°$, $45°$, $90°$). Engineering stress versus strain curves revealed significant elastic and plastic anisotropy, off-axial strain hardening, and noncatastrophic crack propagation within ganoine.

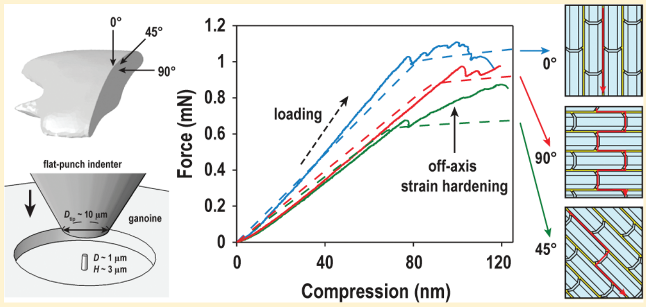

Off-axial compression ($\theta = 45°$) showed the lowest elastic modulus, E (36.2 ± 1.6 GPa, $n \geq 10$, mean $\pm$ SEM), and yield stress, σ_Y (0.81 ± 0.02 GPa), while compression at $\theta = 0°$ showed the highest E (51.8 ± 1.7 GPa) and σ_Y (1.08 ± 0.05 GPa). A 3D elastic−plastic composite nanostructural finite element model revealed this anisotropy was correlated to the alignment of the HAP rods and could facilitate energy dissipation and damage localization, thus preventing catastrophic failure upon penetration attacks.

KEYWORDS: Mechanical anisotropy, energy dissipation, threat protection, uniaxial microcompression, biological exoskeleton, natural armor

A common feature of the outer layer of biological exoskeletons is structural anisotropy which may originate from both "inherent" material anisotropy of the fundamental building blocks, as well as "geometric" anisotropy resulting from the shape, orientation, and spatial distribution of various structural elements.[1−4] The local mechanical properties of such exoskeletal layers have typically been quantified using the technique of nanoindentation,[5−11] using lower loads which induce elastic−plastic deformation, prior to fracture. Nanoindentation, however, produces a heterogeneous multiaxial stress and strain field beneath the indenter,[12] thereby obscuring underlying anisotropy and, in some cases, resulting in direction-independent effective mechanical properties.[13] In our previous work, the predictions of a nanomechanical finite element model[13] were compared to direction-independent nanoindentation data to explore the underlying anisotropic mechanical behavior of a model exoskeletal system, the outermost ∼10 μm ganoine layer of the quad-layered scale armor of the fish, *Polypterus senegalus*[14] (Figure 1a). Ganoine possesses an anisotropic nanocomposite structure composed of ∼95 vol %[15] rodlike hydroxyapatite (HAP) nanocrystals[16] ∼220 nm in length and ∼40 nm in width interacting through rough surfaces and bonded together with thin layers of organic, where the long axis of the HAP rods are oriented approximately perpendicular to the surface plane (Figure 1b).[13] The results of our prior study[13] and others[17,18] suggest that the outer structural anisotropy in multilayered biological systems serves to direct crack propagation, stress, and energy dissipation to greater depths into underlying more ductile material layers, as well as reduce interfacial stresses and, hence, mitigate delamination.

Here, we extend prior work in this area[13,17,18] to *directly* quantify the mechanical anisotropy and fracture of an individual layer of an exoskeleton (i.e., the ganoine of *P. senegalus*) via uniaxial compression. Cylindrical micropillars (∼3 μm high and 1 μm in diameter) of ganoine were prepared using the technique of focused ion beam (FIB) milling[19−23] at different orientations relative to the HAP rod long axis (which coincides with the surface normal[13]). Given that ganoine is highly mineralized, it is particularly resistant to FIB-induced damage,[24] as will be shown later on. Uniaxial compression was conducted on the micropillars using a flat-punch diamond indenter tip which initially induces elastic−plastic deformation, followed by fracture at higher loads. Engineering stress versus strain curves were plotted and the elastic modulus, E, and yield stress, σ_Y, were extracted from these data. The predictions of a previously developed theoretical model of the ganoine composite nanostructure that incorporates the geometrical anisotropy of the rodlike HAP nanocrystals[13] was compared to the experimental data to provide further insights into the underlying mechanical mechanisms and the role of anisotropy in penetration resistance, load-bearing capability, energy dissipation, and fracture.

Individual scales of *P. senegalus* were cut in half with a razor blade. For one set of scale samples, one-half of the scale was designated for compression parallel to the long axis of the rodlike HAP crystals and normal to the scale surface (denoted the 3-direction, $\theta = 0°$, Figure 1a), while the other half was assigned

Received: June 11, 2011
Published: July 14, 2011

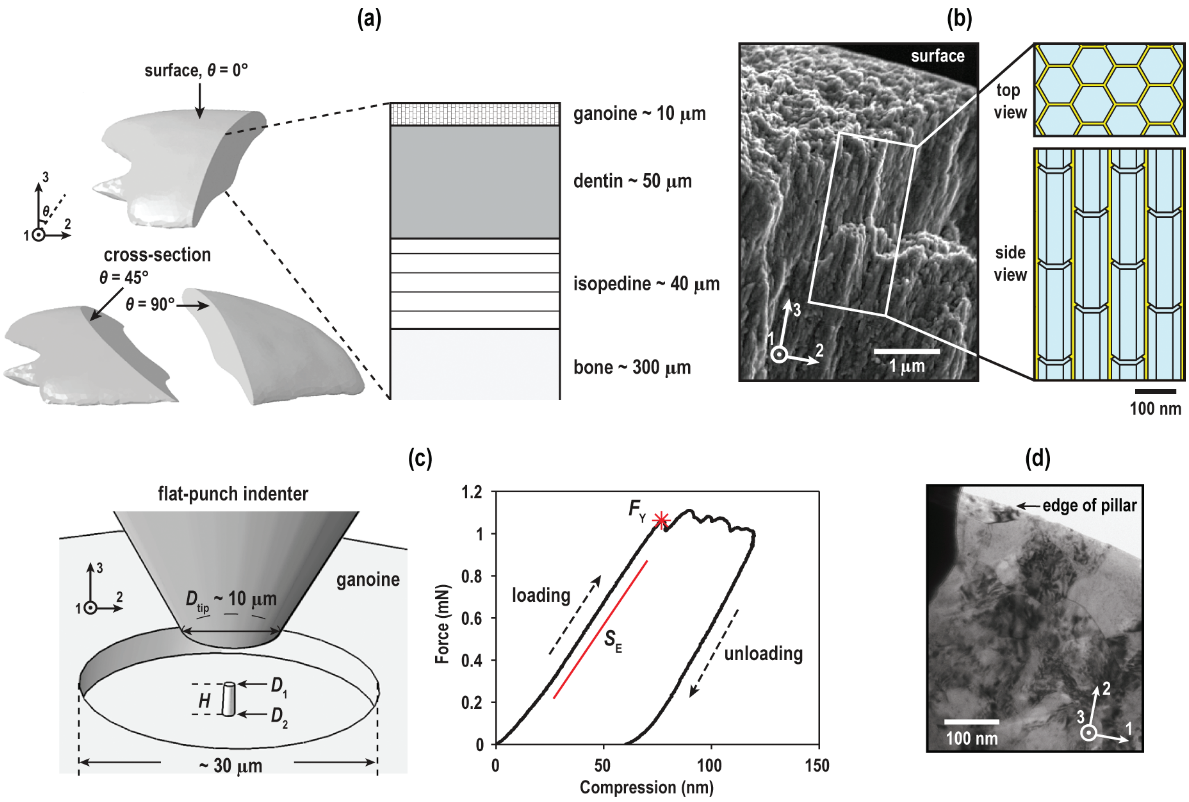

Figure 1. (a) Individual *P. senegalus* scales cut in half, denoting the three directions of a uniaxial microcompression test. Each scale is composed of a juxtaposition of four reinforcing layers.[14] (b) Scanning electron microscope image displays the anisotropic structure of hydroxyapatite−organic nanocomposite ganoine layer.[13] (c) Schematic of uniaxial compression on the micropillar prepared on the ganoine surface using a flat-punch indenter ($D_{tip} \sim 10\ \mu$m). A representative compression curve demonstrates the estimation of force versus compression slope, S_E, and yield force, F_Y. (d) Bright-field transmission electron microscope (TEM) image showing negligible FIB-induced damage at the edge of an individual micropillar. The contrast in the image may arise from defects, organic density distributions, porosity, etc.

for compression perpendicular to 3-direction in the surface plane (denoted the *1,2*-direction, $\theta = 90°$, the material is expected to be transversely isotropic). For the second set of scale samples, they were again cut in half to prepare samples for testing at $\theta = 45°$ to the 3-direction (Figure 1a). The specimens with $\theta = 45°$ and 90° directions were polished stepwise on a polishing wheel (South Bay Technology, model 920, San Clemente, CA) with 1 μm to 100 nm Al_2O_3 particles on adhesive papers (Buehler, Lake Bluff, IL), followed by 50 nm silica nanoparticles on a microcloth pad (Buehler); the 0° specimens were directly polished with the 50 nm silica nanoparticles on a microcloth pad for 5 min to ensure minimal removal of the ganoine layer on the surface (<2 μm, as measured via scanning electron microscopy (SEM, Helios 600, FEI, Hillsboro, OR) after polishing at different time intervals). The surface roughness of all polished samples was found to be <2 nm via tapping mode AFM imaging,[13] much less than the maximum depth of compression (∼120 nm). Cylindrical micropillars were fabricated using the Helios 600 dual-beam focused ion beam (FEI) annular milling[19−23] method at 30 kV applied voltage and a series of decreasing currents (9.3, 0.93, 93, and 48 pA). The dimensions of the micropillars were approximately D_1 (upper face diameter) ∼ 1 μm, H (height) ∼ 3 μm, α (taper angle) ∼ 2.25° (Figure 1c). Each individual micropillar was located in the middle of a crater of ∼30 μm diameter, ∼3 μm height to guarantee the indenter was in contact only with the micropillar and no surrounding material. Uniaxial compression was performed using a flat-punch conical diamond tip (end diameter D_{tip} ∼ 10 μm, cone half angle ∼60°) and a Triboindenter (Hysitron Inc., Minneapolis, MN) in ambient conditions. A depth-controlled closed-looped compression was utilized to maintain a constant 5 nm/s loading/unloading rate up to ∼120 nm compression depth, with 5 s dwell time between the loading and unloading. Prior to each compression test, the flat punch indenter was manually aligned above the pillar using an optical microscope after optics-indenter calibration on an indium sample (99.999%, Alfa Aesar, item 14720, Ward Hill, MA). The number of pillars tested for each direction was $n \geq 10$ with means and standard errors calculated for the mechanical properties, E or σ_Y, measured from these data. Statistical significance was assessed between different orientations using the Mann−Whitney test, and a value of $p < 0.05$ was taken as statistically significant. To assess any possible FIB-induced damage to the ganoine layer, additional micropillars were fabricated in the same fashion and polished into thin slices (<100 nm) following standard transmission electron microscope (TEM) sample preparation procedures. As shown in the bright-field TEM image using a Helios CX200 TEM (FEI), the presence of clear grain boundaries between each of the HAP nanocrystals and absence of any apparent amorphous phase at the edges of the pillar suggested negligible damage to the HAP crystal (Figure 1d), consistent with the literature which reports that HAP is resistant to FIB-induced damage.[24]

From each of the loading portions of the force (F) versus compression depth (δ) curves, the slope, or stiffness of the elastic

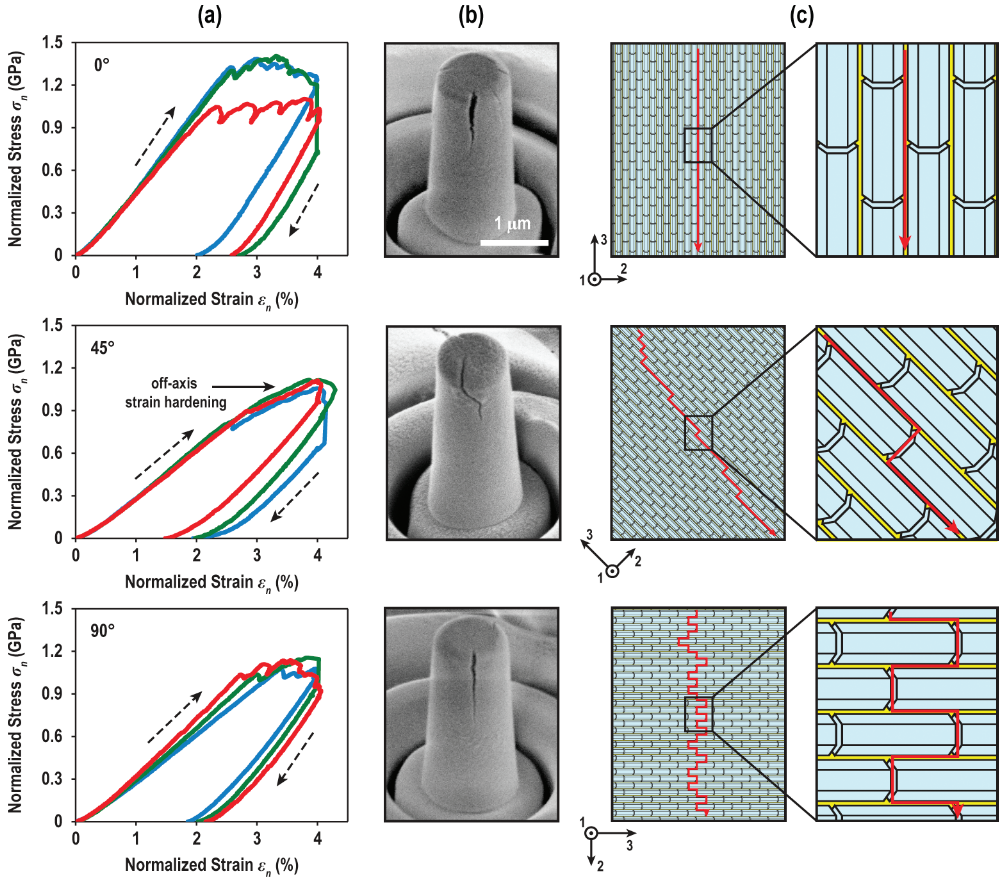

Figure 2. Anisotropic uniaxial compression behavior of ganoine micropillars at θ = 0°, 45°, and 90° to its HAP rod axis (surface normal). (a) Representative normalized engineering stress σ_n versus strain ε_n curves obtained from three individual micropillars for each θ. (b) Typical crack propagation pathways observed via SEM after the compression (shown at a 45° stage tilt). (c) Schematic of crack initiation and propagation mechanisms based on the ganoine nanostructure.

deformation regime, S_E, was measured (Figure 1c). The measured stiffness reflects the combined effect of the compression of the micropillar and the indentation of the pillar into the underlying bulk of ganoine. Applying Sneddon's formula,[25] which accounts for the substrate compliance, the normalized engineering stress σ_n and strain ε_n for the slightly tapered pillars can be estimated as

$$\varepsilon_n = \frac{\delta}{H} \tag{1}$$

$$\sigma_n = \left(\frac{4}{\pi D_1 D_2} + \frac{1-\nu^2}{D_2 H}\right)F \tag{2}$$

where ν is approximated as the average Poisson's ratio of ganoine ($\nu \sim 0.26$),[13] H is the pillar height, and D_1 and D_2 are the diameters of the top and bottom face of the pillar due to the taper angle α, respectively. The elastic modulus, E, was extracted from the elastic portion of the normalized stress versus strain curve via least-squares linear regression ($E = d\sigma_n/d\varepsilon_n$). The force at the yield point F_Y was taken as the first point where the load dropped below 95% of the force predicted by S_E (Figure 1c). The yield stress, σ_Y, was estimated as

$$\sigma_Y = \frac{4F_Y}{\pi {D_1}^2} \tag{3}$$

σ_n versus ε_n compression behavior was observed to be distinctly different for the three different directions tested, thus confirming and quantifying the mechanical anisotropy of ganoine directly (Figure 2a). For each orientation, the σ_n versus ε_n data for different micropillars show excellent repeatability (Figure 2a). Upon uniaxial compressive loading, a linear increase of σ_n with ε_n was observed up to a yield point of $\varepsilon_n \sim 2-3\%$ for all the micropillars. After yielding took place, a jagged, heterogeneous plateau was present for the micropillars at θ = 0° and 90°. In comparison, for micropillars at θ = 45°, σ_n continued to increase with ε_n postyielding due to the strain hardening effect, albeit at a smaller slope than the elastic region. The crack propagation pathways were also direction-dependent, as observed via SEM (Helios 600) after the compression test (Figure 2b). For the pillars with θ = 0° and 90°, the cracks propagated nearly perpendicular to the micropillar surface. For those with θ = 45°, the cracks initiated perpendicular to the surface due to the contact constraint at the pillar top surface and then deviated to ~45° to the surface during the propagation. These observations are consistent with the hypothesis that the failures were initiated and propagated through the relatively more compliant and weaker organic content by shearing between the HAP crystals, as shown in the schematic in Figure 2c. Such noncatastrophic fracture and crack propagation ("graceful failure"), which maintains load-bearing capability after fracture initiation, provides significant energy dissipation, similar to bone.[18] The elastic modulus, E, and yield stress, σ_Y, calculated via the σ_n versus ε_n curves were found to show significant direction dependence via the Mann–Whitney test (Figure 3). The micropillars tested at $\theta = 0°$ were observed to have a significantly higher E and σ_Y since the loading was applied parallel to the long axis of the HAP rods, while the off-axis response ($\theta = 45°$) has the lowest E and σ_Y. In addition, the postyield behavior at off-axis yield retained unique, relatively strong compression resistance, with the measured compressive stiffness of 22.5 ± 1.4 GPa (mean ± SEM, $n \geq 10$ micropillars) calculated in the strain-hardening regime of the σ_n versus ε_n curves (Figure 2a) in the same fashion as the estimation of the elastic modulus, E, which was ~38% reduction from E (Figure 3a).

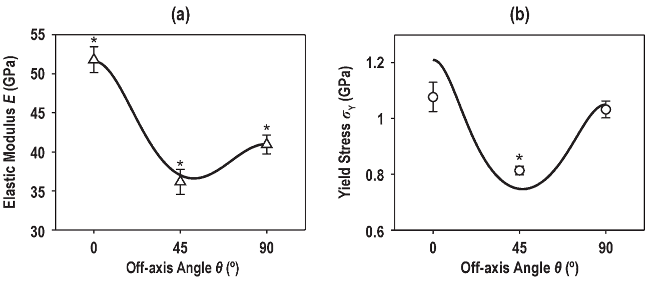

Figure 3. Direction-dependent elastic modulus (E) and yield stress (σ_Y) of ganoine micropillars, showing both the experimental results ($n \geq 10$ pillars for each direction, mean ± SEM) and theoretical predictions. Asterisks suggest statistically significant different E or σ_Y from other two directions (Mann–Whitney test, $p < 0.05$).

A previously reported 3D anisotropic elastic–plastic composite nanomechanical finite element analysis (FEA)-based model[13] was utilized to simulate the nanostructural and nanomechanical features of the ganoine layer. This FEA model takes into account the HAP crystal dimensions and geometry (rodlike nanocrystals length of ~220 nm and width of ~40 nm), orientation, packing, and volume fraction (95 vol %)[16] (Figure 1c). A representative volume element (RVE) was constructed to idealize the imperfectly aligned nanostructure as a periodic arrangement of hexagonally packed HAP rods embedded in an organic matrix, with transverse mineral elements between the rods to simulate the irregular rod-to-rod surface roughness and discontinuity of the organic matrix[13] (Figure 4a). Since the intrinsic anisotropy within the HAP has a minimal effect on the overall mechanical properties of ganoine,[13] the mechanical properties of the HAP crystals were taken to be isotropic with a Young's modulus of 60 GPa, Poisson's ratio of

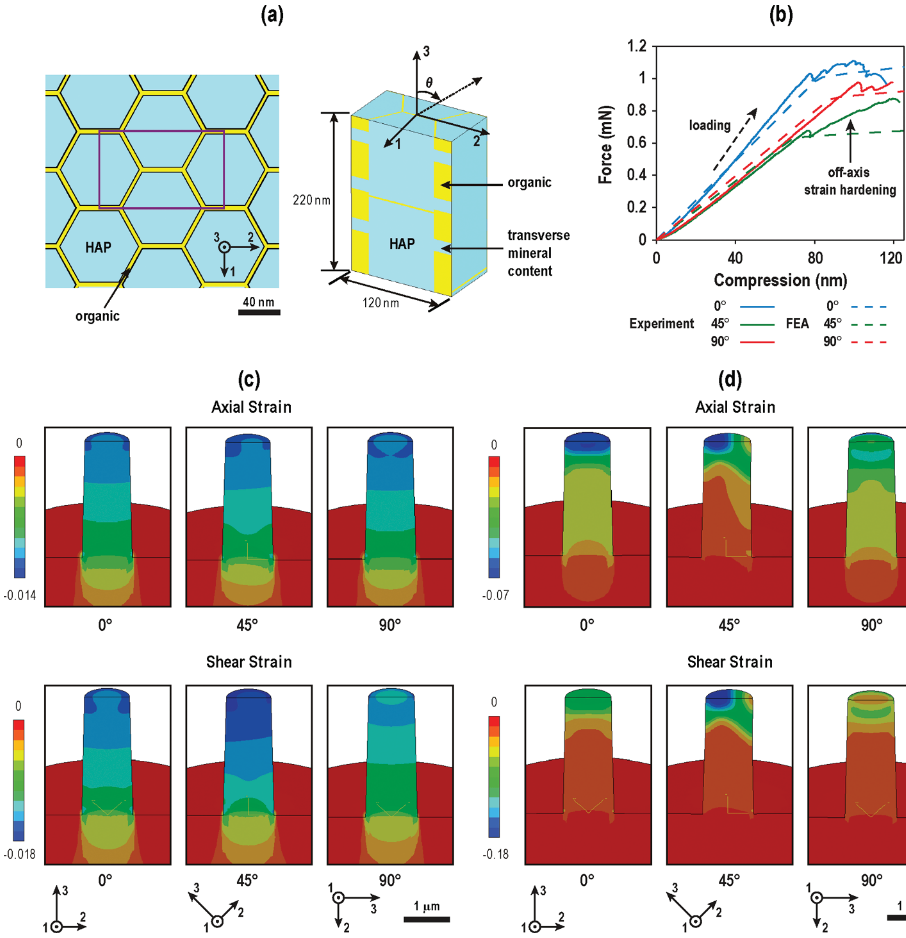

Figure 4. Finite element analysis results on ganoine nanocomposites. (a) RVE of ganoine nanostructure with transverse mineral content to account for the HAP shape irregularity and crystal interlocking. (b) Simulated force–displacement curves of ganoine micropillars at $\theta = 0°$, 45°, and 90° under uniaxial compression as compared with experimental data. Postyield strain hardening was observed at $\theta = 45°$. (c, d) Axial strain and shear strain at the three directions to the HAP long axis at two levels of compression: (c) $\delta = 40$ nm in the elastic deformation region, (d) $\delta = 100$ nm in the plastic deformation region.

Table 1. Predicted Anisotropic Material Constants for Ganoine Layer from Nanomechanical Model of RVE

$E_1 = E_2$ (GPa)	E_3 (GPa)	$G_{13} = G_{23}$ (GPa)	G_{12} (GPa)	ν_{12}	$\nu_{32} = \nu_{31}$	$\sigma_{Y,1} = \sigma_{Y,2}$ (GPa)	$\sigma_{Y,3}$ (GPa)	$\tau_{Y,13} = \tau_{Y,23}$ (GPa)	$\tau_{Y,12}$ (GPa)
41	51.6	13.5	15.4	0.28	0.25	1.05	1.21	0.4	0.61

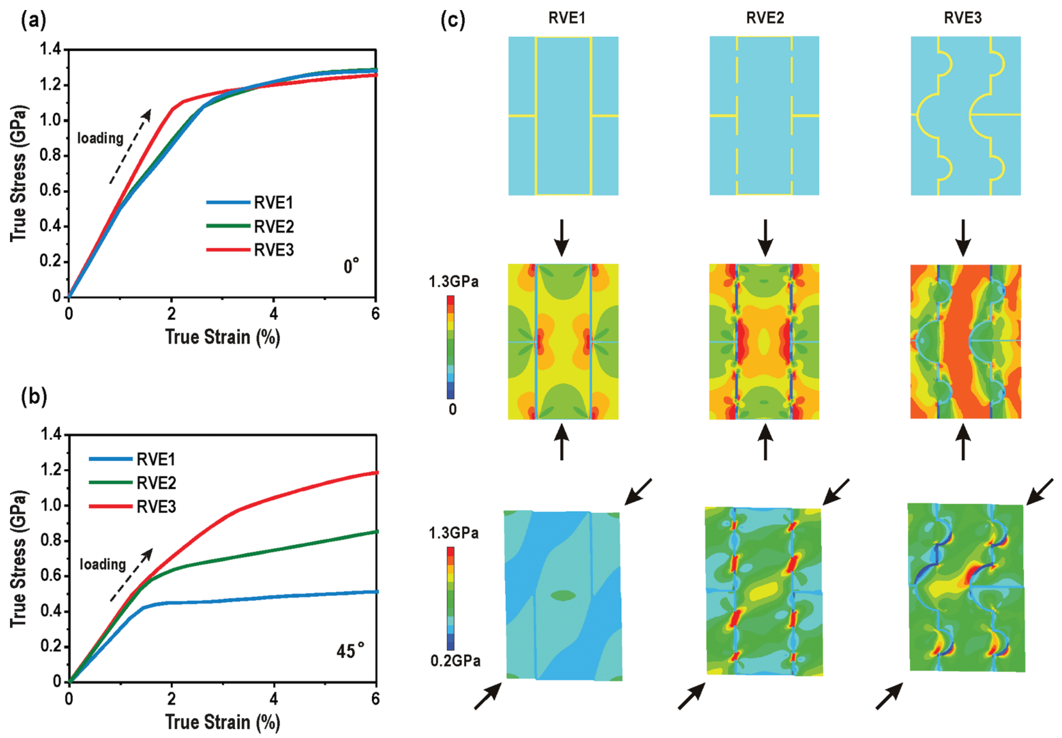

Figure 5. Finite element analysis showing the comparison between three 2D representative volume elements: RVE1 considers an ideal brick-and-mortar structure of HAP prisms bonded by the organic layer; RVE2 considers the organic layer continuity to be interrupted by transverse mineral elements; RVE3 considers adjacent HAP prisms with rough interlocking surface. (a) Stress−strain response of the RVEs under uniaxial compression at $\theta = 0°$. (b) Stress−strain response of the RVEs under uniaxial compression at $\theta = 45°$. (c) Geometry and the corresponding von Mises stresses of the three RVEs under uniaxial compression at $\theta = 0°$ and $\theta = 45°$ at 2% compressive strain.

0.3, and a yield stress of 1.3 GPa. In addition, the mechanical properties of the organic matrix were approximated by a Young's modulus of 4.3 GPa, Poisson's ratio of 0.3, and a yield stress of 0.4 GPa.[13] The HAP material properties used in the nanomechanical FEA model simulations were scaled down to be lower than those of ideal HAP crystal properties. For biological samples, it is expected that the modulus of HAP does not reach the ideal value (∼120 GPa[26,27]) since its chemical composition, purity, and the presence of porosity all act to reduce the intrinsic mechanical properties. For example, the modulus of HAP crystals in bone is ∼80 GPa,[28] significantly lower than the ideal value. Regarding ganoine, the HAP crystals are one order of magnitude larger in physical dimension than those in bone (HAP crystals in bone have a cross-section dimension of 1−5 nm and axial length of 25−50 nm[28]). Given the larger size of the HAP crystallites in ganoine compared to bone, a larger degree of intercalated organic/porosity within each of the single crystal is expected and likely reflected in the heterogeneous contrast observed in the TEM images taken on the cross section of an individual micropillar (Figure 1d). These defects are expected to further reduce the modulus and yield strength.[29−31] Four simulations were conducted on the RVE (two uniaxial compressions and two simple shears) to determine all anisotropic material properties. The simulated stress−strain responses show strong directional dependence of the macroscopic response of the ganoine nanocomposite (data not shown). Table 1 provides the full set of anisotropic material constants for the ganoine layer predicted from the nanomechanical modeling, showing modest elastic anisotropy and anisotropic yield with a low off-plane shear yield strength.

To estimate the material strength based on nanomechanical properties, the Hill quadratic anisotropic yield criterion was used. The uniaxial yield strength σ_Y is direction-dependent and given as a function of the angle θ of loading to the primary material axis (axis 3 in Figures 1, 2, and 4) of orthotropy[32]

$$\frac{\sigma_Y^2 \cos^4\theta}{X_1^2} + \frac{\sigma_Y^2 \sin^4\theta}{X_2^2} + \frac{\sigma_Y^2 \sin^2\theta \cos^2\theta}{X_{12}^2} - \frac{\sigma_Y^2 \sin^2\theta \cos^2\theta}{X_1^2} = 1 \quad (4)$$

where X_1 and X_2 are the yield stresses parallel and perpendicular to the primary material axis, respectively, and X_{12} is the shear yield stress. The elastic modulus was also estimated in a similar manner

$$E(\theta) = \frac{1}{S_{11}\cos^4\theta + (2S_{12} + S_{66})\sin^2\theta\cos^2\theta + S_{22}\sin^4\theta} \quad (5)$$

where S_{11} and S_{22} are the elastic compliances parallel and perpendicular to the primary material axis, S_{12} is the off-diagonal compliance tensor component, and S_{66} is the shear compliance. The model prediction of E and σ_Y as a function of loading orientation agreed well with the experimental observation, as depicted in Figure 3. Therefore, the nanomechanical model successfully describes the major anisotropic mechanical property trends of ganoine. Direct experimental observation of the direction dependence in uniaxial compression behavior (Figure 2b) was provided here to support the hypothesis that the anisotropy of ganoine leads to shear localization within and tortuous crack propagation along the more compliant organic components, thus increasing energy dissipation, increasing penetration resistance, and facilitating protection from external predatory attacks.

Full three-dimensional FEA models of micropillars were then constructed where ganoine was discretized into eight-node linear hybrid brick elements with anisotropic material properties obtained from the RVE model as shown in Table 1. The three orientations of θ = 0°, 45°, and 90° were considered for comparison with the experimental data. Figure 4b shows the corresponding simulated force−displacement curves of ganoine micropillars for these three cases under uniaxial compression. The agreement with the experimental curves indicates the capability of the nanomechanical model to capture the anisotropic behavior of ganoine under compression deformation. Panels c and d of Figure 4 depict the axial and shear strains for each of the three ganoine orientations in the elastic and postyield regions, respectively. All strain contours are found to be symmetric with respect to the axis of the cylindrical micropillars for the θ = 0° and 90° cases at both small and large displacements due to the symmetry of geometry, material, and loading conditions. However, for the case of θ = 45°, this symmetry is broken because of the material orientation. The shear strain is aligned approximately in the 45° direction, indicating oblique deformation in the micropillar which is more pronounced after yield. In this case, the axial strain was partially released since the axial displacement is mainly accommodated by the shear straining of the micropillar. These predictions of shearing localizing along the organic layer are consistent with the eventual propagation of a crack along the organic layer (however, note we have not simulated fracture). In addition, note that the strain in the substrate underneath the micropillars confirms the need to use Sneddon's correction[25] in calculating the elastic modulus.

There exist a number of differences between the nanomechanical RVE (Figure 4a)[13] and the actual ganoine structure. For example, the HAP rods possess some irregularities in shape and surface roughness (Figure 1d), rather than the idealized hexagonal HAP rods. The irregularities and surface roughness are expected to lead to rod-to-rod interlocking. During off-axis loading, the shearing of the interface region can play a significant role in the mechanical response. The interlocking surface provides a marked change in the postyield behavior as compared to the case of the ideal prism geometry. While the transverse mineral features in the original RVE capture the surface roughness effect on initial yield, they do not capture postyield behavior. The postyield strain hardening response for pillars at θ = 45° is speculated to be due to the interlocking and friction between the adjacent prisms. To explore this mechanism, a number of new RVEs were constructed to capture the prism-to-prism irregularity and interlocking effect, as shown in Figure 5. RVE1 considers an ideal brick-and-mortar structure of HAP prisms bonded by the organic layers; RVE2 considers the organic layer continuity to be interrupted by transverse mineral elements; RVE3 considers adjacent HAP prisms with a rough interlocking surface. The enhanced off-axis stiffness, yield stress, and postyield strain hardening behavior are clearly observed in the RVE3 at θ = 45° due to the enhanced shearing resistance by the prism-to-prism interlocking structure, which are not seen in the RVE1 with smooth surface of mineral prisms and are partly accounted for in the RVE2 with transverse mineral elements (see Figure 5b). Different interlocking geometries have negligible influence on the axial stiffness and axial strength (see Figure 5a for θ = 0°). These RVEs emphasize the critical importance of the shape irregularity of structural biological materials at the nanoscale in achieving macroscale anisotropic mechanical properties. These results also suggest the ability to tailor the wavy interfacial geometry to enhance the off-axis yield stress and strain hardening behavior of composites at nano- or microlength scales.[33] For example, the postyield strain hardening of the shear behavior plays a significant role in the nanoindentation and neglecting such hardening leads to an overestimation of yield stress values when reducing from experimental load-depth curves. Therefore, instead of nanoindentation, uniaxial microcompression is used to provide a direct and unambiguous measure of the anisotropic yield behavior.

Furthermore, there may also be a small tilt angle (<5°) between the HAP nanocrystal long axis and the surface normal.[13] As a result, E and σ_Y can be slightly lower for the pillars at θ = 0° and 90°, and slightly higher for those at θ = 45°. In the presented system, however, this effect is minimal, as variation up to 5° in the tilt angle θ leads to reductions in E and σ_Y values much smaller than the standard errors due to the intrinsic variation within the biological system as seen in Figure 3. The only exception is that near θ = 0°, σ_Y is highly sensitive to the tilt angle, which could be part of the reason there was the relatively larger difference between the theoretical and experimental σ_Y measured at θ = 0° (Figure 3b). Other inaccuracies such as possible friction between the diamond punch and the pillar top, the first-mode plastic buckling, and constraint of the pillar by the underlying material are negligible for the pillar dimensions implemented here.[34] Overall, the main conclusions on the effect of anisotropy remain valid with the presence of these aforementioned deviations from the ideal situation assumed in the nanomechanical model.

In this study, the anisotropic mechanical behavior and fracture of the outer ganoine layer of individual *P. senegalus* scales was quantified with uniaxial microcompression tests on specimens produced via FIB-based fabrication technique. The local direction-dependent uniaxial compression behavior of ganoine was interpreted using a nanostructure-specific FEA model that reveals deformation mechanisms, anisotropic stiffness, and yield, postyield, and local stress and strain distributions. The major results are summarized as follows.

(1) The previously predicted reduction in modulus and yield strength off-axis (θ = 45°)[13] was experimentally confirmed (Figure 3). This reduction provides direct evidence of the anisotropic response within ganoine, which serves to facilitate plastic shearing, dissipate energy, and localize the damage during penetration attacks to avoid radial crack propagation that leads to catastrophic failure.

(2) Crack propagation pathway was directly observed to correlate with the alignment of HAP rods (Figure 2b). Upon a multiaxial penetration attack, the observed crack propagation pathways suggest that cracks tend to propagate along the organic layers[13] (Figure 2c) and result in localized fracture that can easily be suppressed by the underlying, ductile dentin layer.

(3) The resulting strain hardening and tortuous crack propagation pathways (Figure 2) reveal the important role of the interlocking prism roughness in providing postyield hardening in shear and off-axis loading. This interlocking due to irregular shape of HAP crystals effectively increases intercrystal frictions that promotes energy dissipation during crack propagation.

(4) While the local anisotropy is clearly advantageous, ganoine simultaneously exhibits direction-independent multiaxial indentation behavior[13] (the expected mode of predatory attack),[9,35] which is also advantageous so that there are no weaker angles of attack.

This study is expected to be relevant to other biological systems which exhibit structural anisotropy.[1−4,18] For example, human teeth are composed of an outer enamel layer that has similar HAP crystals perpendicular to the surface embedded in organic material,[17] where the structural anisotropy could provide similar function to prevent catastrophic failure. The information obtained from this study can serve for use as fundamental design principles for biomimetic systems of synthetic human body armor. For example, for a ballistic composite human body armor, an outermost layer with vertically aligned hard ceramic or metallic nanocrystals embedded in soft materials can mimic the design of ganoine, and facilitate to promote energy dissipation and prevent catastrophic failure.

AUTHOR INFORMATION

Corresponding Author
*E-mail: cortiz@mit.edu.

ACKNOWLEDGMENT

The authors are grateful for the support of the MIT Institute for Soldier Nanotechnologies (Contract DAAD-19-02-D0002), the National Science Foundation MIT Center for Materials Science and Engineering (DMR-0819762), the National Security Science and Engineering Faculty Fellowship (N00244-09-1-0064), and the MIT Nanomechanical Technology Laboratory. The authors also thank Dr. J. R. Greer (California Institute of Technology) for valuable discussions and Dr. A. F. Schwartzman, Dr. S. Chen, and Dr. Y. Zhang for technical assistance.

REFERENCES

(1) Al-Sawalmih, A.; Li, C.; Siegel, S.; Fabritius, H.; Yi, S.; Raabe, D.; Fratzl, P.; Paris, O. *Adv. Funct. Mater.* **2008**, *18*, 3307–3314.
(2) Chateigner, D.; Hedegaard, C.; Wenk, H.-R. *J. Struct. Geol.* **2000**, *22*, 1723–1735.
(3) Parsons, A. H. *Poult. Sci.* **1982**, *61*, 2013–2021.
(4) Rodríguez-Navarro, A. B.; CabraldeMelo, C.; Batista, N.; Morimoto, N.; Alvarez-Lloret, P.; Ortega-Huertas, M.; Fuenzalida, V. M.; Arias, J. I.; Wiff, J. P.; Arias, J. L. *J. Struct. Biol.* **2006**, *156*, 355–362.
(5) Li, X.; Chang, W.-C.; Chao, Y. J.; Wang, R.; Chang, M. *Nano Lett.* **2004**, *4*, 613–617.
(6) Bruet, B. J. F.; Qi, H. J.; Boyce, M. C.; Ortiz, C. *J. Mater. Res.* **2005**, *20*, 2400–2419.
(7) Sachs, C.; Fabritius, H.; Raabe, D. *J. Mater. Res.* **2006**, *21*, 1987–1995.
(8) Sun, J.-Y.; Tong, J.; Ma, Y.-H. *J. Bionic Eng.* **2008**, *5*, 152–157.
(9) Bruet, B. J. F.; Song, J.; Boyce, M. C.; Ortiz, C. *Nat. Mater.* **2008**, *7*, 748–756.
(10) Yao, H.; Dao, M.; Imholt, T.; Huang, J.; Wheeler, J.; Bonilla, A.; Suresh, S.; Ortiz, C. *Proc. Natl. Acad. Sci. U.S.A.* **2010**, *107*, 987–992.
(11) Lian, J.; Wang, J. Microstructure and mechanical properties of dungeness crab exoskeletons. In *Mechanics of Biological Systems and Materials, Vol. 2, Proceedings of the 2011 Annual Conference on Experimental and Applied Mechanics*; Proulx, T., Ed.; Springer: New York, 2011; pp 93−99.
(12) Swadener, J. G.; Rho, J.-Y.; Pharr, G. M. *J. Biomed. Mater. Res., Part A* **2001**, *57*, 108–112.
(13) Wang, L.; Song, J.; Ortiz, C.; Boyce, M. C. *J. Mater. Res.* **2009**, *24*, 3477–3494.
(14) Daget, J.; Gayet, M.; Meunier, F. J.; Sire, J.-Y. *Fish. Fish.* **2001**, *2*, 113–124.
(15) Ørvig, T., Phylogeny of tooth tissues: Evolution of some calcified tissues in early vertebrates. In *Structural and Chemical Organization of Teeth*; Miles, A. E. W., Ed.; Academic Press: New York and London, 1967; Vol. 1, pp 45−110.
(16) Meunier, F. J. *Arch. Zool. Exp. Gén.* **1980**, *122*, 279.
(17) Habelitz, S.; Marshall, S. J.; Marshall, G. W. Jr.; Balooch, M. *Arch. Oral Biol.* **2001**, *46*, 173–183.
(18) Seto, J.; Gupta, H. S.; Zaslansky, P.; Wagner, H. D.; Fratzl, P. *Adv. Funct. Mater.* **2008**, *18*, 1905–1911.
(19) Uchic, M. D.; Dimiduk, D. M.; Florando, J. N.; Nix, W. D. *Science* **2004**, *305*, 986–989.
(20) Greer, J. R.; Oliver, W. C.; Nix, W. D. *Acta Mater.* **2005**, *53*, 1821–1830.
(21) Greer, J. R.; Jang, D.; Kim, J.-Y.; Burek, M. J. *Adv. Funct. Mater.* **2009**, *19*, 2880–2886.
(22) Kim, J.-Y.; Jang, D.; Greer, J. R. *Acta Mater.* **2010**, *58*, 2355–2363.
(23) Greer, J. R.; De Hosson, J. Th.M. *Prog. Mater. Sci.* **2011**, *56*, 654–724.
(24) Volkert, C. A.; Busch, S.; Heiland, B.; Dehm, G. *J. Microsc.* **2004**, *214*, 208–212.
(25) Sneddon, I. N. *Int. J. Eng. Sci.* **1965**, *3*, 47–57.
(26) Zhang, C.; Leng, Y.; Chen, J. *Biomaterials* **2001**, *22*, 1357–1363.
(27) Arias, J. L.; Mayor, M. B.; Pou, J.; Leng, Y.; León, B.; Pérez-Amor, M. *Biomaterials* **2003**, *24*, 3403–3408.
(28) Fritsch, A.; Hellmich, C. *J. Theor. Biol.* **2007**, *244*, 597–620.
(29) Posner, A. S.; Betts, F. Molecular control of tissue mineralization. In *Chemistry and Biology of Mineralized Connective Tissues*; Veis, A., Ed.; Elsevier: Amsterdam, 1981; pp 257−266.
(30) Leventouri, T. *Biomaterials* **2006**, *27*, 3339–3342.
(31) Weiner, S. *Bone* **2006**, *39*, 431–433.
(32) Hill, R. *Proc. R. Soc. London* **1948**, *193*, 281–297.
(33) Barthelat, F.; Tang, H.; Zavattieri, P. D.; Li, C.-M.; Espinosa, H. D. *J. Mech. Phys. Solids* **2007**, *55*, 306–337.
(34) Zhang, H.; Schuster, B. E.; Wei, Q.; Ramesh, K. T. *Scr. Mater.* **2006**, *54*, 181–186.
(35) Song, J.; Ortiz, C.; Boyce, M. C. *J. Mech. Behav. Biomed. Mater.* **2011**, *4*, 699–712.